Zaltoprofen / 4,4'-Bipyridine: a case study to demonstrate the potential of differential scanning calorimetry (DSC) in the pharmaceutical field

Giovanna Bruni[a]*, Lauretta Maggi[b], Francesco Monteforte[a], Chiara Ferrara[c], Doretta Capsoni[a], Vittorio Berbenni[a], Chiara Milanese[a], Alessandro Girella[a], Valeria Friuli[b], Piercarlo Mustarelli[c] and Amedeo Marini[a].

[a] C.S.G.I. - Department of Chemistry, Physical-Chemistry Section, University of Pavia, Via Taramelli 16, 27100 Pavia, Italy
[b] Department of Drug Sciences, University of Pavia, Via Taramelli 12, 27100 Pavia, Italy
[c] Department of Materials Science, University of Milano-Bicocca, via Cozzi 55, 20125 Milano, Italy

* Corresponding author:
Giovanna Bruni; ORCID: 0000-0003-1958-2998
Tel.: +39 0382 987667; e-mail: giovanna.bruni@unipv.it

Keywords: Differential scanning calorimetry, Thermodynamic model, Cocrystals, Zaltoprofen/ 4,4'-Bipyridine, Spectroscopic characterization (XRPD, FT-IR, SS-NMR), Solubility and dissolution rate.

ABSTRACT

The Zaltoprofen/4,4'-Bipyridine system gives rise to two co-crystals of different compositions both endowed - in water and in buffer solution at pH 4.5 - with considerably higher solubility and dissolution rate than the pure drug.

The qualitative and quantitative analysis of the DSC measurements, carried out on samples made up of mixtures prepared according to different methodologies, allows us to elaborate and propose an accurate thermodynamic model that fully takes into account the qualitative aspects of the complex experimental framework and which provides quantitative predictions (reaction enthalpies and compositions of the co-crystals) in excellent agreement with the experimental results. Co-crystal formation and cocrystal compositions were confirmed by X-ray diffraction measurements as well as by FT-IR and NMR spectroscopy measurements.

The quantitative processing of DSC measurements rationalizes and deepens the scientific aspects underlying the so-called Tammann's triangle and constitutes a model of general validity. The work shows that DSC has enormous potential, which however can be fully exploited only by paying adequate attention to the experimental aspects and the quantitative processing of the measurements.

1. INTRODUCTION

The aim of this paper is to demonstrate the often underestimated potential of differential scanning calorimetry (DSC) in the pharmaceutical field and in particular in the study of the interactions in the multicomponent systems containing active principles.

~~This work has two aims: 1) to improve the pharmaceutical behavior of an active principle through the formation of co-crystals with a suitable coformer; 2) to demonstrate the often underestimated potential of differential scanning calorimetry (DSC) in the pharmaceutical field.~~

To successfully pursue this goal we have chosen the binary solid system consisting of zaltoprofen, and the coformer 4,4'-bipyridine. This system gives rise to two co-crystals of different compositions, both characterized by complex thermal behavior, which can be considered excellent model compounds for the study of pharmaceutical co-crystals (4,4'-bipyridine is toxic and is unsuitable for pharmaceutical application).

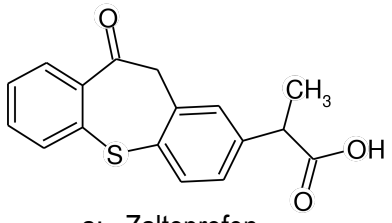

a: Zaltoprofen

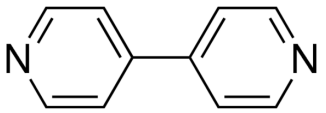

b: 4,4'-Bipyridine

Scheme 1 – Molecular structures of zaltoprofen and 4,4'-bipyridine.

Zaltoprofen [2-(10, 11-dihydro-10-oxodibenzo [b, f] thiepin-2-yl) propionic acid, scheme 1a] is a potent non-steroidal anti-inflammatory drug belonging to the propionic acid class. It has analgesic, antipyretic and anti-inflammatory activity and is used in the treatment of acute and chronic inflammation, rheumatoid arthritis and post-operative pain.[1,2] It is well tolerated orally compared to other NSAIDs, and it is administered with a dose of 80 mg in three or four doses per day. This active principle is practically insoluble in water (it belongs to Class II of the Biopharmaceutics Classification System) and, since enhanced bioavailability and a rapid onset are desirable properties for analgesics, there is a strong scientific and clinical interest in the preparation of novel forms with higher water solubility and dissolution rate.

Co-crystals are an efficient and trendy expedient to tailor the physico-chemical properties of drugs and in particular to enhance the solubility and dissolution rate of poorly water-soluble active principles so that their absorption from the gastro-intestinal tract can be improved and the desired therapeutic benefits can be reached in short times.[3,4] Co-crystals are defined as crystalline single-phase materials made by two different molecules, the drug and the coformer, in a definite stoichiometric ratio. They are formed through short-range non-covalent interactions such as hydrogen bonds and van der Waals interactions and may show improved pharmaceutical behavior over the starting components as a consequence of a different crystal packing.[5-8]

4,4'-Bipyridine (scheme 1b) is one of the most frequently used coformers for the formation of co-crystals because of the presence of the pyridine group in its molecule.[9] Indeed, since the carboxyl-pyridine heterosynthon is a highly probable supramolecular synthon, co-crystals with this molecule have been reported for a number of common drugs such as ibuprofen,[10] felodipine[11], paracetamol[12] and acetylsalicylic acid[10]. Thus, we chose it as coformer for the co-crystallization with zaltoprofen due to its potential to form hydrogen bond with the carboxylic acid group.[13]

The co-crystallization can be induced in solution, by mechanical activation and also by heating, so that these multicomponent entities can be synthetized by different methods: solution-based methods (evaporative crystallization, cooling crystallization, slurry technique), solid-state based methods (neat and liquid-assisted grinding, extrusion), spray-drying and freeze-drying.[14,15]

The proper characterization of solid systems of pharmaceutical interest requires the use of different investigation techniques.[3,16] In this work DSC measurements were the primary source of information, supported by FT-IR spectroscopy, X-ray powder diffraction (XRPD) and solid-state nuclear magnetic resonance (SS-NMR) measurements. Solubility and dissolution rate measurements were also performed. All these techniques contributed to the understanding of this system but, as anticipated, the most important contribution came from DSC measurements.

Although differential scanning calorimetry is widely used in pharmaceutical research in the study of solid systems, almost always it is used at a level lower than that which the potential of the investigation technique would make possible. The modest level concerns both the experimental aspects, related to the preparation of samples and the execution of measurements, and the theoretical aspects, related to the processing of the results of the measurements.[17-22] We aim here to demonstrate, by devoting attention to both aspects, that it is possible to obtain information that could hardly be obtained with other investigation techniques.

Quite often the physico-chemical behavior of binary systems of pharmaceutical interest is rather complex; the system zaltoprofen/4,4'-bipyridine is particularly complex and therefore constitutes an excellent test bed to illustrate the potential of the DSC technique.

2. MATERIALS AND METHODS

2.1 MATERIALS AND SAMPLES PREPARATION

Zaltoprofen (purity 99%, *Z* hereinafter) and 4,4'-bipyridine (purity 97%, *B* hereinafter), were purchased from Sigma-Aldrich Company (Milan, Italy).

Binary systems with different compositions were prepared in two different ways: 1) by mixing the two components in a Turbula mixer (Willy-Bachofen, Basel, Switzerland) for 10 minutes (imput speed of the motor axis 46 rpm). The samples obtained in this way will be named *TM* hereinafter; 2) by manually kneading the powders with the addition of a few drops of ethanol. The samples were allowed to dry at room atmosphere 3 days. They will be named *KN* hereinafter.

2.2 PHYSICO-CHEMICAL CHARACTERIZATION

2.2.1 Thermal measurements

A DSC Q2000 apparatus interfaced with a TA 5000 data station (TA Instruments, New Castle, DE, USA) was used to perform thermal analyses. The calibration of the DSC instrument was performed using ultrapure indium (99.999%; melting point = 156.6 °C; melting enthalpy = 28.54 $J \cdot g^{-1}$) as standard. The samples (about 3.5-4 mg) were scanned heating at 1 $K \cdot min^{-1}$ under nitrogen flow (45 $ml \cdot min^{-1}$) in open standard aluminum pans. 1 $K \cdot min^{-1}$ is a rather low heating rate and is certainly much lower than that routinely used for DSC measurements, but it is the best choice if the goal is to maximize the resolution of the measurement (i.e., to separate otherwise overlapping peaks) and/or to advance the reactive processes that occur during heating to the maximum degree.

2.2.2 XRPD measurements

A powder diffractometer D5005 Bruker (Karlsruhe, Germany) (Cu Kα radiation, λ(Kα1) = 1.54046 Å; voltage of 40 kV and current of 40 mA), equipped with a θ-θ vertical goniometer, Ni filter, monochromator, and scintillation counter was used. The patterns were collected at room temperature in step scan mode (step size: 0.020°, counting time: 3 s per step) in the $5 < 2\theta° < 35$ angular range.

2.2.3 FT-IR measurements

FT-IR measurements were performed by a Nicolet FT-IR iS10 Spectrometer (Nicolet, Madison, WI, USA) equipped with ATR (Attenuated Total Reflectance) sampling accessory (Smart iTR with diamond plate) and 32 scans in the 4000–550 cm^{-1} range with resolution set at 4 cm^{-1} were co-added.

2.2.4 NMR measurements

Solid state NMR data were collected on an Avance III Bruker 400 MHz spectrometer (9.4 T magnet) using a 4 mm MAS probe. ^{1}H spectra were collected with a single-pulse sequence adopting a π/2 pulse of 2.5 ms and averaging over 128 scans under MAS condition (10 kHz). ^{13}C spectra were acquired with ^{1}H-^{13}C CPMAS sequence under the same MAS condition. ^{1}H π/2 pulse was 2.5 ms, delay time 5-200 s depending on the sample, as previously determined with ^{1}H experiments, contact time 2.5 ms, and the signals were averaged over 1k-8k acquisitions for CP under MAS condition (10 kHz). Chemical shifts for both ^{1}H and ^{13}C have been referred to adamantane signals as secondary standard respect to tetramethyl silane (TMS, 0 ppm). All spectra were acquired, processed and analyzed with the package Topspin 3.1 (Bruker).

2.2.5 Solubility and dissolution test measurements

The solubilities of *Z* and of *KN* samples with composition x_Z = 0.25, 0.66, 0.80 (x_Z is the molar fraction of Z in the binary mixture) were determined in deionized water and in a pH 4.5 phosphate buffer solution (simulating fed conditions) at 21°C, using the shake-flask method. At time intervals, an aliquot of the saturated solutions was sampled, filtered (0.22 μm; Millipore), properly diluted,

and the Zaltoprofen concentration was determined by spectrophotometric detection (Lambda 25 UV Winlab V6 software; Perkin Elmer, Monza, Italy). We report the results obtained after two hours (because the drug should be in solution in a very short time to be absorbed and promptly effective) and then the solubility at equilibrium (mean of three measurements) that is reached in about 24-36 hours. The pH of media was measured during the test.

The dissolution tests were performed using the dissolution test apparatus 2, paddle (Erweka DT-D6, Dusseldorf, Germany) at 37.0 ± 0.5°C, 50 rpm, in 900 mL of pH 6.8 phosphate buffer, according to the monograph of *Z* described in the Japanese Pharmacopoeia.[23] The test was performed also in two other dissolution media: pH 4.5 buffer, to simulate the administration with food, and deionized water (three replicas). The amount of drug dissolved was determined by UV detection at 338 nm with a calibration curve previously performed, (spectrophotometer Lambda 25; Perkin Elmer). The data analysis was performed by a suitable software (Winlab V6 software, Perkin Elmer, Monza, Italy). All samples contained the same amount of *Z* (80 mg) and were previously sieved through a 230 mesh grid (63μm).

3. RESULTS AND DISCUSSION

3.1 DSC MEASUREMENTS

3.1.1. Preliminary considerations on DSC measurements

Figure 1 shows, as an example, the DSC traces of some *TM* and *KN* mixtures of different composition. The DSC curve of the starting materials (*Z* and *B*) are presented in figure S1.

The *KN* samples were prepared and examined in order to have additional information on the behavior of the system. If, in fact, it can be assumed that the method of preparation of *TM* samples (mixing in Turbula at room temperature) does not lead to any strong interaction between the components, the kneading can lead, already at room temperature, to interactions between components that would only occur at higher temperatures.

A tangible example of the fact that the *KN* preparation produced different effects on the sample than simple mixing in Turbula can be obtained from the comparison of figures 1a, a* and 1b, b*, which show the DSC traces of *TM* and *KN* samples of identical composition: the evident endo-exo effect (T_{onset} = 72 °C) present in the *TM* samples is completely absent in the *KN* samples. On the other hand, the sharp endothermic peak with T_{onset} = 87 °C which in *TM* samples immediately follows the endo-exo effect is clearly present also in *KN* samples.

Having observed that the DSC traces of *TM* and *KN* samples are different from each other, we must take note that both change significantly as the composition varies (see figure 2). It is therefore worth analyzing them in detail to try to identify the physico-chemical processes at the origin of the thermal effects.

3.1.2. Qualitative analysis of the measurements performed on the mixtures $0.10 \leq x_Z \leq 0.40$

The qualitative analysis of the DSC measurements of these mixtures is reported in detail in the supplementary material. Here we summarize only the indications obtained from this analysis:

- The endo/exo effect that is recorded on *TM* samples (but is absent in *KN* samples) is due to the fusion of a metastable eutectic (*EU1**) from which co-crystals *CC1* are formed;
- In *KN* samples *CC1* co-crystals are quantitatively formed already at room temperature as a consequence of the preparation method;
- The endothermic peak with T_{onset} = 87 ° C, present in both *TM* and *KN* samples, is due to the melting of a stable eutectic *EU2* formed by *CC1* and *B*.
- *EU2* has a composition close to x_Z = 0.25 (corresponding to a mass percentage of *Z*, %*Z* = 38.90) and melting enthalpy close to 77.5 $J \cdot g^{-1}$;
- *CC1* and *EU2* have very similar compositions.

3.1.3. Quantitative analysis of the endothermic peak with T_{onset} = 87 °C

The values obtained for the specific melting enthalpy (*TM* samples) are plotted as a function of the nominal composition of the mixture analyzed in Figure 3 (red points and red interpolating lines).
The one shown in figure 3 is a so-called Tammann's diagram. We already discussed [24-25] the rationale behind the Tammann's diagram and we remember here only that the composition and the specific melting enthalpy of the eutectic mixture *EU2* are identified by the abscissa and ordinate of the intersection point of the two interpolating lines.
The elaboration of our measurements provides the following results (coordinates of the intersection point):

- the composition of *EU2* is: $\%Z = Z_{EU2}^{\%} = 38.45$;
- the specific melting enthalpy of *EU2* is: $\Delta H_{EU2}^{th} = 78.1\ \mathrm{J} \cdot \mathrm{g}^{-1}$.

We recall, before continuing, that the composition x_Z = 0.25 that our qualitative analysis (*KN* samples) indicated as close to the composition of *EU2*, corresponds to %*Z* = 38.90 and that the melting enthalpy of *EU2* deduced from the qualitative analysis was close to 77.5 $J \cdot g^{-1}$. Therefore, both the composition and the melting enthalpy of *EU2* deduced from the measurements on the *KN* sample x_Z = 0.25 are in good agreement with the results obtained from the processing of all the data relating to the melting peak of *EU2* in *TM* samples and confirm that the measurements performed on mixtures prepared with the *KN* method can be of great help for the understanding of solid systems of pharmaceutical interest. The result obtained also explains our previous statement about the fact that the compositions of *CC1* and *EU2* are very similar. We believe that the composition of *CC1* is %*Z* = 38.90, corresponding to a molar ratio *Z*:*B* = 1:3. However, our Tammann's diagram shows that the negative slope line intersects the abscissa axis – and therefore the specific enthalpy measured for the melting of *EU2* vanishes – for %*Z* = 80.87 rather than for %*Z* = 100.00 as it should be. This means that the expected negative line is certainly different from the experimental one. It is therefore worth checking whether this also happens for the expected and experimental lines with a positive slope.

To construct the expected lines, we need to know their analytic equations. The problem was already dealt with in detail [25] and here we report only the final result and the meaning of the symbols used.

$$\Delta \boldsymbol{H}_{\boldsymbol{EU2}}^{\boldsymbol{exp}} = \Delta \boldsymbol{H}_{\boldsymbol{EU2}}^{\boldsymbol{th}} \cdot \frac{\boldsymbol{m}_{\boldsymbol{EU2}}}{\boldsymbol{m}_{\boldsymbol{s}}} = \Delta \boldsymbol{H}_{\boldsymbol{EU2}}^{\boldsymbol{th}} \cdot \frac{\%\boldsymbol{Z} \cdot \left(\mathbf{1} + \frac{\boldsymbol{B}_{\boldsymbol{EU2}}^{\%}}{\boldsymbol{Z}_{\boldsymbol{EU2}}^{\%}}\right)}{\mathbf{100}} = \%\boldsymbol{Z} \cdot \left[\frac{\Delta \boldsymbol{H}_{\boldsymbol{EU2}}^{\boldsymbol{th}} \cdot \left(\mathbf{1} + \frac{\boldsymbol{B}_{\boldsymbol{EU2}}^{\%}}{\boldsymbol{Z}_{\boldsymbol{EU2}}^{\%}}\right)}{\mathbf{100}}\right] \quad (1)$$

(1) is the analytical equation of the expected line with a positive slope.

$$\Delta \boldsymbol{H}_{\boldsymbol{EU2}}^{\boldsymbol{exp}} = \Delta \boldsymbol{H}_{\boldsymbol{EU2}}^{\boldsymbol{th}} \cdot \frac{\boldsymbol{m}_{\boldsymbol{EU2}}}{\boldsymbol{m}_{\boldsymbol{s}}} = \Delta \boldsymbol{H}_{\boldsymbol{EU2}}^{\boldsymbol{th}} \cdot \frac{(\mathbf{100} - \%\boldsymbol{Z}) \cdot \left(\mathbf{1} + \frac{\boldsymbol{Z}_{\boldsymbol{EU2}}^{\%}}{\boldsymbol{B}_{\boldsymbol{EU2}}^{\%}}\right)}{\mathbf{100}} = -\frac{\%\boldsymbol{Z}}{\mathbf{100}} \cdot \Delta \boldsymbol{H}_{\boldsymbol{EU2}}^{\boldsymbol{th}} \cdot \left(\mathbf{1} + \frac{\boldsymbol{Z}_{\boldsymbol{EU2}}^{\%}}{\boldsymbol{B}_{\boldsymbol{EU2}}^{\%}}\right) + \Delta \boldsymbol{H}_{\boldsymbol{EU2}}^{\boldsymbol{th}} \cdot \left(\mathbf{1} + \frac{\boldsymbol{Z}_{\boldsymbol{EU2}}^{\%}}{\boldsymbol{B}_{\boldsymbol{EU2}}^{\%}}\right) \quad (2)$$

(2) is the analytical equation of the expected line with a negative slope.

In equations (1) and (2):

$\Delta \boldsymbol{H}_{\boldsymbol{EU2}}^{\boldsymbol{exp}}$ is the expected value of the specific melting enthalpy (J·g^{-1} sample) of the eutectic mixture in the analyzed sample;

$\Delta \boldsymbol{H}_{\boldsymbol{EU2}}^{\boldsymbol{th}}$ is the value of the specific melting enthalpy (J·g^{-1} sample) of the eutectic mixture in the sample of eutectic composition;

$\boldsymbol{m}_{\boldsymbol{EU2}}$ is the mass of eutectic mixture *EU2* present in the analyzed sample;

$\%\boldsymbol{Z}$ is the percentage by mass of *Z* present in the analyzed sample;

$\boldsymbol{B}_{\boldsymbol{EU2}}^{\%}$ is the percentage by mass of *B* predicted by the composition of *EU2*. It is a constant that depends exclusively on the composition of *EU2*;

$\boldsymbol{Z}_{\boldsymbol{EU2}}^{\%}$ is the mass percentage of *Z* predicted by the composition of *EU2*. It is a constant that depends exclusively on the composition of *EU2*.

To construct the expected straight lines, we will use the values of $Z_{EU2}^{\%} = 38.45$ and $\Delta H_{EU2}^{th} = 78.1\ \mathrm{J \cdot g^{-1}}$ obtained from our measurements. Obviously $B_{EU2}^{\%} = 100 - Z_{EU2}^{\%}$. The expected lines are also shown in Figure 3 (black points and black interpolating lines). As can be seen, the experimental (red line) and expected (black line) positive slope lines are almost coincident. The lines with a negative slope, on the other hand, are quite different. There is clearly a thermodynamic constraint by virtue of which there is no formation of *EU2* in mixtures of composition %*Z* ≥ 80.87: therefore, the experimental line (red line) discounts a thermodynamic constraint not foreseen by the calculated line (black line). We will now try to find the analytical equation of the expected line in the presence of the thermodynamic constraint. The question concerns exclusively the line with a negative slope since there is no thermodynamic constraint for the line with a positive slope.

To insert the thermodynamic constraint in the calculation of the expected values for the negative slope line, we will assume that the constraint on the formation of *CC1* (and then of *EU2*) operates for compositions %*Z* > 38.45, i.e., for compositions with a content of *Z* higher than that of *EU2*, and totally inhibits the formation of *CC1* (and then of *EU2*) for compositions %*Z* ≥ 80.87.

3.1.4. The thermodynamic constraint

In the absence of any thermodynamic constraint, we would have:

$$\boldsymbol{m_{EU2}} = \%\boldsymbol{B} + \%\boldsymbol{B} \cdot \frac{\boldsymbol{Z^{\%}_{EU2}}}{\boldsymbol{B^{\%}_{EU2}}} = \%\boldsymbol{B} \cdot \left(\mathbf{1} + \frac{\boldsymbol{Z^{\%}_{EU2}}}{\boldsymbol{B^{\%}_{EU2}}}\right) \quad (3)$$

The logic of equation (3) is quite simple:

a. The mass of *EU2* is given by the sum of the masses of its components;
b. Since *B* is the defective component, the entire amount of *B* (%*B*) present in the mixture will form *EU2*;
c. The mass of *Z* (excess component) that forms *EU2* will obviously be linked to that of *B* because the composition of *EU2* is defined and provides for a defined molar ratio – and therefore a defined mass ratio – between the components *B* and *Z*. It follows that the mass of *Z* that forms *EU2* will be given by the mass of *B* multiplied by the mass ratio between *Z* and *B* in *EU2*.

In the absence of any thermodynamic constraint, the entire amount of *B* (the defective component) would form *EU2*, so that it will be enough to replace %*B* with the nominal % content of *B* in the mixture. However, in the presence of a thermodynamic constraint, which operates for compositions %*Z* > 38.45, it is no longer true that the entire amount of *B* (the component in defect) forms *EU2*: a portion of *B* now does not participate in the formation of *EU2*. We must find an active concentration value $B^{\#}$ which, inserted in (3), allows us to obtain the correct value of $\boldsymbol{m_{EU2}}$ and, from this, the correct value of the expected melting enthalpy. Therefore, the introduction of the thermodynamic constraint transforms (3) into:

$$\boldsymbol{m_{EU2}} = \%\boldsymbol{B}^{\#} + \%\boldsymbol{B}^{\#} \cdot \frac{\boldsymbol{Z^{\%}_{EU2}}}{\boldsymbol{B^{\%}_{EU2}}} = \%\boldsymbol{B}^{\#} \cdot \left(\mathbf{1} + \frac{\boldsymbol{Z^{\%}_{EU2}}}{\boldsymbol{B^{\%}_{EU2}}}\right) \quad (4)$$

The following considerations allow us to derive the active concentration $B^{\#}$.

- In the limit mixture of nominal composition %*B* = 19.13 (corresponding to %*Z* = 80.87 and x_Z = 0.689) the amount of *B* useful for the formation of *EU2*, i.e. the active concentration of *B,* is zero ($\%B^{\#}$ = 0.00) because no *EU2* is formed at all.
- In the limit mixture at the opposite end, i.e. in the limit mixture of nominal composition *EU2*, the nominal amount of *B* is 61.55% and coincides with the quantity useful for the formation of *EU2*, i.e. with the active concentration of *B* ($\%B^{\#} = \%B$).
- The difference between the nominal content of *B* which coincides with that useful for the formation of *EU2* ($\%B^{\#} = \%B$ when $\%B = B^{\%}_{EU2} = 61.55$) and the nominal content of *B* when there is no formation of *CC1/EU2* ($\%B^{\#} = 0$ when $\%B = B^{\%}_{x_Z=0.689} = 19.13$), is: $\boldsymbol{B^{\%}_{EU2} - B^{\%}_{x_Z=0.689} = 61.55 - 19.13}$.
- Starting from the extreme in which the nominal content and the useful content of *B* coincide ($\%B^{\#} = \%B = B^{\%}_{EU2} = 61.55$) the active concentration $\%B^{\#}$ will be linked to the nominal content of *B* by the following relationship:

$$\%\boldsymbol{B}^{\#} = \%\boldsymbol{B} - (\mathbf{61.55} - \%\boldsymbol{B}) \cdot \frac{\mathbf{19.13}}{\mathbf{61.55 - 19.13}} \quad (5)$$

In general, using symbolic terms, equation (6) can be written:

$$\%\boldsymbol{B}^{\#} = \%\boldsymbol{B} - \left(\boldsymbol{B}^{\%}_{\boldsymbol{EU2}} - \%\boldsymbol{B}\right) \cdot \frac{\boldsymbol{B}^{\%}_{\boldsymbol{x_Z=0.689}}}{\boldsymbol{B}^{\%}_{\boldsymbol{EU2}} - \boldsymbol{B}^{\%}_{\boldsymbol{x_Z=0.689}}} \quad (6)$$

From the point of view of the physical meaning, equation (6) homogeneously distributes in the whole range of nominal compositions 19.13 < %*B* < 61.55 the limit reduction of the active concentration of *B* and therefore calculates for each mixture of nominal composition %*B*, the active concentration %*B*#, i.e. the percentage of *B* that forms *CC1/EU2*. The substitution of (6) into (4) leads to:

$$\boldsymbol{m_{EU2}} = \left[\%\boldsymbol{B} - \frac{\boldsymbol{B}^{\%}_{\boldsymbol{x_Z=0.689}}}{\boldsymbol{B}^{\%}_{\boldsymbol{EU2}} - \boldsymbol{B}^{\%}_{\boldsymbol{x_Z=0.689}}} \cdot \left(\boldsymbol{B}^{\%}_{\boldsymbol{EU2}} - \%\boldsymbol{B}\right)\right] \cdot \left(1 + \frac{\boldsymbol{Z}^{\%}_{\boldsymbol{EU2}}}{\boldsymbol{B}^{\%}_{\boldsymbol{EU2}}}\right) \quad (7)$$

Substituting the pertinent numerical values in (7):

$\boldsymbol{B}^{\%}_{\boldsymbol{x_Z=0.689}} = \boldsymbol{19.13}$

$\boldsymbol{B}^{\%}_{\boldsymbol{EU2}} = \boldsymbol{61.55}$

$\boldsymbol{Z}^{\%}_{\boldsymbol{EU2}} = \boldsymbol{38.45}$

We obtain:

$$\boldsymbol{m_{EU2}} = \left[\%\boldsymbol{B} - \frac{\boldsymbol{19.13}}{\boldsymbol{61.55 - 19.13}} \cdot \left(\boldsymbol{61.55} - \%\boldsymbol{B}\right)\right] \cdot \left(\boldsymbol{1} + \frac{\boldsymbol{38.45}}{\boldsymbol{61.55}}\right) \quad (8)$$

$$\boldsymbol{m_{EU2}} = \%\boldsymbol{B} \cdot \boldsymbol{2.36} - \boldsymbol{45.10} \quad (8')$$

$$\Delta\boldsymbol{H}^{\boldsymbol{exp}}_{\boldsymbol{EU2}} = \Delta\boldsymbol{H}^{\boldsymbol{th}}_{\boldsymbol{EU2}} \cdot \frac{\boldsymbol{m_{EU2}}}{\boldsymbol{m_s}} = \frac{\Delta\boldsymbol{H}^{\boldsymbol{th}}_{\boldsymbol{EU2}}}{\boldsymbol{100}} \cdot \left(\%\boldsymbol{B} \cdot \boldsymbol{2.36} - \boldsymbol{45.10}\right) \quad (9)$$

Equation (9) allows us to calculate the expected values $\Delta\boldsymbol{H}^{\boldsymbol{exp}}_{\boldsymbol{EU2}}$ in the presence of the thermodynamic constraint. Figure 4 shows the excellent agreement between the experimental line with a negative slope (red points) and the one calculated with the thermodynamic constraint (green line): the two lines overlap, which means the thermodynamic constraint is operating.

The analytical equation of the green line with a negative slope will be discussed in more detail later.

3.1.5. Qualitative analysis of the measurements performed on the x_Z > 0.40 mixtures

The qualitative analysis of the DSC measurements on these mixtures is reported in detail in the supplementary material and we summarize here only the indications obtained from the analysis:

- for compositions 38.45 <% *Z* < 80.87 new *CC2* cocrystals are formed together with *CC1* ones;
- the composition of *CC2* co-crystals is x_Z = 0.66 (corresponding to %*Z* = 79.25), the specific melting enthalpy is 87.1 J·g^{-1} and the melting temperature is T_{onset} = 127 °C;
- For compositions %*Z* > 79.25 a new eutectic *EU4* is formed by *CC2* and *Z*.
- *EU4* has composition at x_Z = 0.80 (corresponding to %*Z* = 88.43), melting enthalpy close to 88 J·g^{-1} and T_{onset} at 118 °C.

3.1.6. Quantitative analysis of the endothermic peak with T_{onset} = 118 °C

A second endothermic peak with measurable area, and therefore susceptible of quantitative analysis, is that with T_{onset} = 118 °C which is present only in mixtures with composition %*Z* > 80.87. We remember that our qualitative analysis attributed such a peak to the melting of a eutectic

mixture *EU4* formed by *CC2* and *Z* and with probable composition at %*Z* = 88.43, corresponding to x_Z = 0.80. As for the composition of *CC2*, we have slightly different indications depending on whether we consider the data obtained from the measurements on the *TM* samples (Tammann's diagram for *EU2*) or those provided by the measurements on the *KN* samples. In the first case, the composition of *CC2* corresponds to that of the sample for which the melting enthalpy of *EU2* is zeroed (see figure 3, intersection of the experimental line with negative slope with the abscissa axis): $\%Z = Z_{CC2}^{\%} = 80.87$. The measurements on the *KN* samples indicate instead that the composition of *CC2* is $Z_{CC2}^{\%} = 79.25$.

Now the quantitative analysis of the melting peak of *EU4* allows us to obtain the experimental values of both the composition and the specific melting enthalpy of this eutectic mixture. It also allows us to obtain a new assessment of the composition of *CC2*, which will correspond to the composition for which the value of the specific melting enthalpy of *EU4* is canceled. The comparison between the composition value of *CC2* that we will obtain from the quantitative analysis of the melting peak of *EU4* and that we have obtained from the quantitative analysis of the melting peak of *EU2* (composition for which the specific melting enthalpy of *EU2* vanishes) will provide an excellent basis for evaluating the self-consistency of our experimental data.

The measurements used for the quantitative analysis of the *EU4* melting peak were performed on the *KN* samples because these samples gave much more reproducible results than those obtained from the *TM* samples. The processing of our measurements on the melting peak of *EU4* provides the following results (coordinates of the intersection point of the lines shown in Figure 5 and intersection with the abscissa axis of the positive slope line):

- the composition of *EU4* is %*Z* = 89.03 (abscissa of the intersection point)
- the specific melting enthalpy of *EU4* is $\Delta H_{EU4}^{th} = 94.9\ \mathrm{J \cdot g^{-1}}$ (ordinate of the intersection point)
- $\Delta H_{EU4}^{th} = 0.0\ \mathrm{J \cdot g^{-1}}$ for %*Z* = 81.02 (intersection with the abscissa axis of the positive slope line).

Since, as we have anticipated, the composition of *CC2* is that for which the specific melting enthalpy of *EU4* vanishes, the composition of *CC2* obtained from the quantitative analysis of the melting peak of *EU4* is $\%Z = Z_{CC2}^{\%} = 81.02$. This value is very close to that obtained from the quantitative analysis of the melting peak of *EU2*, confirming that our experimental data are optimally self-consistent.

Now, if we want to compare the expected and experimental trends of the specific enthalpies of the melting peak of *EU4*, it is necessary, similarly to what we did for *EU2*, to calculate the amounts of *EU4* that can be formed in the different mixtures analyzed and, from these, the expected values of the specific melting enthalpy. In other words, we have to find, as we did for *EU2*, the analytical equations of the expected lines ΔH_{EU4}^{exp} vs %*Z*.

For mixtures with composition %*Z* > 81.02, the *Z* component is in excess of the composition of *CC2*, therefore the entire amount of *B* present in the mixture forms *CC2*:

$$\boldsymbol{m_{CC2}} = \%\boldsymbol{B} + \%\boldsymbol{B} \cdot \frac{\boldsymbol{Z^{\%}_{CC2}}}{\boldsymbol{B^{\%}_{CC2}}} = \%\boldsymbol{B} \cdot \left(\mathbf{1} + \frac{\boldsymbol{Z^{\%}_{CC2}}}{\boldsymbol{B^{\%}_{CC2}}}\right) \quad (10)$$

$\boldsymbol{m_{CC2}}$ is the mass of *CC2* co-crystals present in the analyzed sample;

$\%\boldsymbol{B}$ is the percentage by mass of *B* present in the analyzed sample; it represents the total mass percentage of *B*, regardless of whether *B* is present in free form or is contained in *CC2*;

$\boldsymbol{B^{\%}_{CC2}}$ is the percentage by mass of *B* predicted by the composition of *CC2*. It is a constant that depends exclusively on the composition of *CC2*;

$\boldsymbol{Z^{\%}_{CC2}}$ is the percentage by mass of *Z* predicted by the composition of *CC2*. It is a constant that depends exclusively on the composition of *CC2*.

For these mixtures in which only *CC2* and *Z* are present, it must also apply:

$$\boldsymbol{m_Z} = \mathbf{100} - \boldsymbol{m_{CC2}} \quad (11)$$

For mixtures with 81.02 < %*Z* < 89.03, *CC2* is in excess with respect to the composition of *EU4* and the mass of *EU4* that can be formed is limited by the component in defect, i.e. *Z*:

$$\boldsymbol{m_{EU4}} = \boldsymbol{m_Z} + \boldsymbol{m_Z} \cdot \frac{\boldsymbol{CC2^{\%}_{EU4}}}{\boldsymbol{Z^{\%}_{EU4}}} = \boldsymbol{m_Z} \cdot \left(\mathbf{1} + \frac{\boldsymbol{CC2^{\%}_{EU4}}}{\boldsymbol{Z^{\%}_{EU4}}}\right) = \boldsymbol{m_Z} \cdot \frac{\mathbf{100}}{\boldsymbol{Z^{\%}_{EU4}}} \quad (12)$$

$\boldsymbol{m_{EU4}}$ is the mass of eutectic mixture *EU4* present in the analyzed sample;

$\boldsymbol{m_Z}$ is the mass of *Z* which did not form *CC2*;

$\boldsymbol{CC2^{\%}_{EU4}}$ is the percentage by mass of *CC2* predicted by the composition of *EU4*. It is a constant that depends exclusively on the composition of *EU4* and its value is 57.81%;

$\boldsymbol{Z^{\%}_{EU4}}$ is the mass percentage of *Z* predicted by the composition of *EU4*. It is a constant that depends exclusively on the composition of *EU4* and its value is 42.19%

Equation (12) allows us to calculate the mass of *EU4* that can be formed when *Z* is the component in defect: as %*Z* increases, said mass will increase until it reaches its maximum value in the mixture of composition *EU4*. Therefore (12) will allow us to calculate the expected values of the melting enthalpy for the positive slope line of the Tammann's graph.

For mixtures with composition %*Z* > 89.03 the *Z* component continues to be in excess with respect to *CC2*, therefore it still happens that the entire amount of *B* present in the samples forms *CC2* and $\boldsymbol{m_{CC2}}$ is obtained again from (10).

For these mixtures, however, *CC2* is at a lower level than predicted by the composition of *EU4* and it is *CC2* that limits the amount of *EU4* that can be formed:

$$\boldsymbol{m_{EU4}} = \boldsymbol{m_{CC2}} + \boldsymbol{m_{CC2}} \cdot \frac{\boldsymbol{Z^{\%}_{EU4}}}{\boldsymbol{CC2^{\%}_{EU4}}} = \boldsymbol{m_{CC2}} \cdot \left(\mathbf{1} + \frac{\boldsymbol{Z^{\%}_{EU4}}}{\boldsymbol{CC2^{\%}_{EU4}}}\right) = \boldsymbol{m_{CC2}} \cdot \frac{\mathbf{100}}{\boldsymbol{CC2^{\%}_{EU4}}} \quad (13)$$

Equation (13) allows us to calculate the mass of *EU4* that can be formed when *Z* is the excess component: as %*Z* increases, %*B* decreases and – since *B* is the limiting component for the formation of *CC2* – m_{CC2} decreases and m_{EU4} also decreases until it is canceled out for %*Z* = 100.00. Therefore (13) will allow us to calculate the expected values of the specific melting enthalpy for the negative slope line of the Tammann's graph.

Remembering that:

$$\Delta \boldsymbol{H}_{\boldsymbol{EU4}}^{\boldsymbol{exp}} = \Delta \boldsymbol{H}_{\boldsymbol{EU4}}^{\boldsymbol{th}} \cdot \frac{\boldsymbol{m_{EU4}}}{\boldsymbol{m_s}}$$

With (10), (11) and (12), taking into account that for mixtures of any composition it must be:

$$\%\boldsymbol{B} + \%\boldsymbol{Z} = \mathbf{100} \tag{14}$$

We get, for the positive slope line:

$$\Delta \boldsymbol{H}_{\boldsymbol{EU4}}^{\boldsymbol{exp}} = \frac{\Delta \boldsymbol{H}_{\boldsymbol{EU4}}^{\boldsymbol{th}}}{\mathbf{100}} \cdot \left(1 + \frac{\boldsymbol{CC2}_{\boldsymbol{EU4}}^{\%}}{\boldsymbol{Z}_{\boldsymbol{EU4}}^{\%}}\right) \cdot \%\boldsymbol{Z} \cdot \left(1 + \frac{\boldsymbol{Z}_{\boldsymbol{CC2}}^{\%}}{\boldsymbol{B}_{\boldsymbol{CC2}}^{\%}}\right) - \Delta \boldsymbol{H}_{\boldsymbol{EU4}}^{\boldsymbol{th}} \cdot \frac{\boldsymbol{Z}_{\boldsymbol{CC2}}^{\%}}{\boldsymbol{B}_{\boldsymbol{CC2}}^{\%}} \cdot \left(1 + \frac{\boldsymbol{CC2}_{\boldsymbol{EU4}}^{\%}}{\boldsymbol{Z}_{\boldsymbol{EU4}}^{\%}}\right) \tag{15}$$

~~The~~ (15) is the analytical equation of the expected line with a positive slope.

From equations (10), (13) and (14) we obtain, for the line with negative slope:

$$\Delta \boldsymbol{H}_{\boldsymbol{EU4}}^{\boldsymbol{exp}} = -\%\boldsymbol{Z} \cdot \frac{\Delta \boldsymbol{H}_{\boldsymbol{EU4}}^{\boldsymbol{th}} \cdot \mathbf{100}}{\boldsymbol{CC2}_{\boldsymbol{EU4}}^{\%} \cdot \boldsymbol{B}_{\boldsymbol{CC2}}^{\%}} + \frac{\Delta \boldsymbol{H}_{\boldsymbol{EU4}}^{\boldsymbol{th}} \cdot \mathbf{10^4}}{\boldsymbol{CC2}_{\boldsymbol{EU4}}^{\%} \cdot \boldsymbol{B}_{\boldsymbol{CC2}}^{\%}} \tag{16}$$

~~The~~ (16) is the analytical equation of the expected line with a negative slope.

The values to be entered in equations 15 and 16 to calculate the points of the expected lines are: $CC2_{EU4}^{\%} = 57.81$; $Z_{EU4}^{\%} = 42.19$; $Z_{CC2}^{\%} = 81.02$; $B_{CC2}^{\%} = 18.98$; $\Delta H_{EU4}^{th} = 94.9$ J·g^{-1}.

The expected lines are shown (together with the experimental ones) in figure 5. We think that the agreement between experimental and expected lines can be considered fairly good.

As we have observed, the composition of *CC2* deduced from the measurements on the *KN* samples is $Z_{CC2}^{\%} = 79.25$. This value is close to those we obtained from the quantitative analysis of the melting peaks of *EU2* ($Z_{CC2}^{\%} = 80.87$) and *EU4* ($Z_{CC2}^{\%} = 81.02$). This confirms that a careful set up of the experimental DSC measurements, in particular sample preparation methodology, can provide important contributions to the qualitative and quantitative understanding of physico-chemical processes.

3.1.7. Comments on the *CC2/EU4* model

The model developed for *EU4* corresponds to a simple eutectic phase diagram with components *CC2* and *Z*. This implies that *CC2* is quantitatively present in all mixtures of composition %*Z* ≥ 80.87. This, in turn, has the consequence that in the mixtures with composition %*Z* > 38.45 (corresponding to the experimental composition of *EU2*) we have formation of *CC2*. The amount of *CC2* formed progressively increases as %*Z* increases (and correspondingly the amount of *CC1* that could theoretically be formed on the basis of the composition of the mixture decreases) until, for %*Z* = 80.87, the formation of *CC2* becomes quantitative, in the sense that the mixture consists exclusively of *CC2*. This is what we have previously called thermodynamic constraint to the formation of *CC1*: the thermodynamic constraint to the formation of *CC1* is constituted by the formation of *CC2*. The formation of *CC2* involves both *B* and *Z* and that is why the active concentrations of *B* and *Z* in the formation of *CC1*/*EU2* are lower - as we have seen - than the nominal values. If %*Z* in the mix grows beyond the composition of *CC2* (therefore %*Z* > 80.87),

there is no longer any competition with *CC1* because only *CC2* can be formed: the active concentrations of the components (for the purpose of forming *CC2*) coincide with the nominal concentrations and the amount of *CC2* present in the mixture is always the maximum compatible with the composition of the mixture. In light of the overall model (the thermodynamic constraint to the formation of *CC1*, and then of *EU2*, is constituted by the formation of *CC2*), equations (6), (7) and (9) relating to *EU2*, can conveniently be written:

$$\%\boldsymbol{B}^{\#} = \%\boldsymbol{B} - \left(\boldsymbol{B}^{\%}_{\boldsymbol{EU2}} - \%\boldsymbol{B}\right) \cdot \frac{\boldsymbol{B}^{\%}_{\boldsymbol{CC2}}}{\boldsymbol{B}^{\%}_{\boldsymbol{EU2}} - \boldsymbol{B}^{\%}_{\boldsymbol{CC2}}} \qquad (6^{*})$$

$$\boldsymbol{m}_{\boldsymbol{EU2}} = \left[\%\boldsymbol{B} - \frac{\boldsymbol{B}^{\%}_{\boldsymbol{CC2}}}{\boldsymbol{B}^{\%}_{\boldsymbol{EU2}} - \boldsymbol{B}^{\%}_{\boldsymbol{CC2}}} \cdot \left(\boldsymbol{B}^{\%}_{\boldsymbol{EU2}} - \%\boldsymbol{B}\right)\right] \cdot \left(\mathbf{1} + \frac{\boldsymbol{Z}^{\%}_{\boldsymbol{EU2}}}{\boldsymbol{B}^{\%}_{\boldsymbol{EU2}}}\right) \qquad (7^{*})$$

$$\Delta\boldsymbol{H}^{\boldsymbol{exp}}_{\boldsymbol{EU2}} = -\%\boldsymbol{Z} \cdot \frac{\Delta\boldsymbol{H}^{\boldsymbol{th}}_{\boldsymbol{EU2}}}{\boldsymbol{B}^{\%}_{\boldsymbol{EU2}} - \boldsymbol{B}^{\%}_{\boldsymbol{CC2}}} + \frac{\Delta\boldsymbol{H}^{\boldsymbol{th}}_{\boldsymbol{EU2}}}{\boldsymbol{B}^{\%}_{\boldsymbol{EU2}} - \boldsymbol{B}^{\%}_{\boldsymbol{CC2}}} \cdot \left(\mathbf{100} - \boldsymbol{B}^{\%}_{\boldsymbol{CC2}}\right) \qquad (9^{*})$$

~~The~~ (9*) is the equation of the green line with a negative slope of figure 4. Therefore:

Slope: $-\frac{\Delta\boldsymbol{H}^{\boldsymbol{th}}_{\boldsymbol{EU2}}}{\boldsymbol{B}^{\%}_{\boldsymbol{EU2}} - \boldsymbol{B}^{\%}_{\boldsymbol{CC2}}}$

Intercept: $\frac{\Delta\boldsymbol{H}^{\boldsymbol{th}}_{\boldsymbol{EU2}}}{\boldsymbol{B}^{\%}_{\boldsymbol{EU2}} - \boldsymbol{B}^{\%}_{\boldsymbol{CC2}}} \cdot \left(\mathbf{100} - \boldsymbol{B}^{\%}_{\boldsymbol{EU2}}\right)$

By substituting the pertinent values in the slope and intercept:

$\Delta\boldsymbol{H}^{\boldsymbol{th}}_{\boldsymbol{EU2}} = \mathbf{78.1}\,;\ \boldsymbol{B}^{\%}_{\boldsymbol{EU2}} = \mathbf{61.55}\,;\quad \boldsymbol{B}^{\%}_{\boldsymbol{CC2}} = \mathbf{19.13}\,,$ we get:

Expected Slope: $-\frac{\mathbf{78.1}}{\mathbf{61.55-19.13}} = \mathbf{-1.84}$

Expected Intercept: $\frac{\mathbf{78.1}}{\mathbf{61.55-19.13}} \cdot (\mathbf{100 - 19.13}) = \mathbf{148.88}$

The experimental values of the red line with negative slope are the same within the experimental error. This is the reason why, as we noted in paragraph 3.1.5, the red and green lines of figure 4 are superimposed.

3.1.8. Summary of DSC measurements

We can summarize the processes and quantities deduced from the DSC measurements as follows:

- *EU1** is a metastable eutectic with T_{onset} = 72 °C. Its thermal effect manifests as an endo-exo peak in *TM* samples but does not appear in *KN* samples (see supplementary material).
- *CC1* are co-crystals with composition x_Z = 0.25. Their melting T_{onset} is 88 °C. The *CC1* melting peak is barely visible in *TM* samples but absent in *KN* ones.
- *EU2* is a stable eutectic. Its melting T_{onset} is 87 °C. The composition of *EU2* is very similar to that of *CC1*. The *EU2* melting peak is visible in both *TM* and *KN* samples. The *EU2* specific melting enthalpy was obtained both from single measurements on *KN* samples (77.5 $J \cdot g^{-1}$) and from the processing of all relevant measurements performed on *TM* samples (78.1 $J \cdot g^{-1}$).
- *EU3** is another metastable eutectic, with T_{onset} = 108 °C. Its thermal effect manifests as an endo-exo peak in *TM* samples but does not appear in *KN* samples (see supplementary material).

- *CC2* are co-crystals with composition different from that of *CC1*. Their melting T_{onset} is 127 °C. Composition ($Z^{\%}_{CC2} = 79.25$) and specific melting enthalpy (87.1 J·g^{-1}) were obtained from measurements on *KN* samples of only two different compositions. Slightly different compositions were obtained from measurements performed on all pertinent *TM* and *KN* samples: $Z^{\%}_{CC2} = 80.87$ and $Z^{\%}_{CC2} = 81.02$ respectively.
  Here we point out that the formation of co-crystals between zaltoprofen and 4,4' bipyridine with the same composition (*Z*:*B* = 2:1) is confirmed by a very recent study of S.G. Dash and T.S. Thakur[26] who determined their crystallographic structure.
- *EU4* is another stable eutectic, melting T_{onset} 118 °C. The *EU4* melting peak is visible in both *TM* and *KN* samples. Composition and specific melting enthalpy of *EU4* were obtained both from measurements on single *KN* samples (%*Z* = 88.43; $\Delta H^{th}_{EU4} = 88.0\ \mathrm{J \cdot g^{-1}}$) and from all relevant measurements performed on *KN* samples (%*Z* = 89.02; $\Delta H^{th}_{EU4} = 94.9\ \mathrm{J \cdot g^{-1}}$).

In *TM* samples, the formation of *CC1* occurs during the calorimetric scan and is triggered by the fusion of the metastable eutectic *EU1**. In *KN* samples, on the other hand, the formation of *CC1* already occurs at room temperature. In both samples, however, the *CC1* melting peak is not measurable because it is "hidden" almost entirely (*TM* samples) or entirely (*KN* samples) from the *EU2* melting peak.

In *TM* samples, *CC2* formation occurs by liquid-solid and/or solid-solid reaction during calorimetric scanning and does not necessarily reach completeness. In *KN* samples, on the other hand, the formation of *CC2* can already occur quantitatively at room temperature. The specific melting enthalpy of *CC2* can only be obtained from single measurements on *KN* samples because: a) it is not certain that there is quantitative formation of *CC2* in *TM* samples; b) it is not possible to process the pertinent measurements on all *TM* and *KN* samples for this purpose because *CC2* forms a eutectic (*EU4*) whose melting peak precedes and replaces the melting peak of *CC2*.

We believe that these observations fully account for what was stated in the introduction about the fact that only by paying adequate attention to both the experimental aspects of the measurements (in particular, methods of sample preparation and heating rate), and the theoretical ones (quantitative processing of the results) it is possible to fully exploit the potential of differential scanning calorimetry in the study of solid systems of pharmaceutical interest.

3.2. XRPD MEASUREMENTS

3.2.1 Measurements on *TM* and *KN* samples x_Z = 0.25

The XRPD patterns of a *TM* and a *KN* sample x_Z = 0.25 are shown, together with those of *Z* and *B* in figure 6. The most intense peaks of *Z* (2θ = 7.5° and 2θ = 14.0°) are completely absent in *KN* but present, albeit with very low intensity, in *TM* samples. Similarly, the more intense peaks of *B* (2θ = 13.5° and 2θ = 26.0°) are absent in *KN* and present in *TM* samples. Other peaks of *B* (2θ = 17.9°; 2θ = 18.7°; 2θ = 28.0°) are also present in *TM* but absent in *KN* samples. These differences in the diffraction patterns suggest that the *KN* sample consists of a new crystalline phase. This

constitutes indirect confirmation of our thermodynamic model, according to which the *KN* sample is constituted by *CC1* while in the *TM* sample there are mainly free *B* and *Z*. However, some diffraction effects that characterize the *KN* sample differentiating it from its pure components are also present in the *TM* sample. In particular, the peaks at 2θ = 10.7°; 2θ = 13.1°; 2θ = 16.2°; 2θ = 19.1°; 2θ = 27.1°, all absent in the pure components are present – albeit with different intensity – in both *KN* and *TM* samples. These observations, which highlight the structural similarities between *KN* and *TM* samples, combined with the previous ones, which instead highlight the differences, suggest that some interaction between the *Z* and *B* components can also occur following simple mixing in Turbula at room temperature and that its intensity is high enough to lead to the formation – albeit partial and probably only on the surface of the samples – of the *CC1* phase which is obtained quantitatively through the kneading procedure.

3.2.2 Measurements on *TM* and *KN* samples x_Z = 0.66

The XRPD patterns of a *TM* and a *KN* sample x_Z = 0.66 are shown, together with those of *Z* and *B* in figure 7. The most intense peaks of *Z* (2θ = 7.5°, 14.0°) are present, even if with different relative intensities and slightly shifted towards low angles, in the *TM* sample but are completely absent in the *KN* sample. The picture is more complex as regards the diffraction effects attributable to pure *B*. Some of these – shifted slightly to the lower angle (2θ = 12.5°, 19.9°, 21.8°, 23.2°, 25.5°) – are present in both *TM* and *KN* samples. The most intense peaks of *B*, however (2θ = 13.6°, 26.0°) are completely absent in the *KN* sample and only hinted at (almost absent) in the *TM* samples. This suggests that in both samples *B* is no longer present in its original crystallographic form. Furthermore, some peaks not attributable to pure components (2θ = 13.0°, 18.9°, 22.8°, 27.0°) are present exclusively in the *KN* samples.

~~The total disappearance of the more intense diffraction effects of the pure components and the appearance of diffraction effects not attributable to these, suggest that the *KN* sample consists of a new crystalline phase, which according to our thermodynamic model corresponds to *CC2*.~~

We calculated the XRPD pattern from the crystallographic structure determined by S.G. Dash and T.S. Thakur[26] for the co-crystal they synthesized with molar composition *Z*:*B* = 2:1. As it can be seen in figure 7, this pattern is well comparable to that of our sample *KN* x_Z = 0.66. Therefore, this a further confirmation of the validity of our thermodynamic model according to which this sample corresponds to *CC2*.

The permanence of the diffraction effects attributable to pure *Z* and the absence of those exclusive to the new crystalline phase, are compatible with the possibility that the *TM* sample consists of a physical mixture of *Z* and *B* in which no interactions have occurred. However, the fact that the more intense peaks of *B* have almost completely disappeared and that several diffraction effects are common to the *TM* and *KN* samples suggest that the interaction that led to the formation of the new crystalline phase in the *KN* sample occurred – albeit only superficially – in the *TM* sample. This is a similar situation to that described for the samples x_Z = 0.25 and confirms that there is an

interaction at the surface level between *Z* and *B* at room temperature by simple mixing of the powders.

3.2.3 Measurements on *TM* and *KN* samples $x_Z = 0.80$

The XRPD patterns of a *TM* and a *KN* sample $x_Z = 0.80$ are shown, together with those of *Z* and *B* in figure 8. The most intense peaks of *Z* are present, albeit slightly shifted towards low angles, in both *TM* and *KN* samples. In the *TM* sample, however, the intensity of said peaks seems greater than in the *KN* sample. The most intense peaks of *B*, on the other hand, are absent in both the *TM* and in the *KN* sample. In the *KN* sample there are all the diffraction effects attributable to *CC2* (see previous point). However, these diffraction effects are present, albeit to a lesser extent, also in the *TM* sample. According to our thermodynamic model, the *KN* sample should be made up of a mixture of *CC2* and *Z* and is therefore entirely consistent with the predictions that it presents the diffraction effects attributable to *CC2* and *Z*. On the other hand, the presence of peaks attributable to *CC2* in the *TM* sample can be explained by taking into account that, as we have seen, some interaction between *Z* and *B* (leading to ~~surficial~~ surface formation of *CC2*) can occur by simple mixing the powders at room temperature.

3.3. FTIR MEASUREMENTS

FT-IR measurements were performed on *TM* and *KN* samples of composition $x_Z = 0.25, 0.66, 0.80$. The absorption spectra are shown in the supplementary material (figures S2, S3 and S4). A common feature of all compositions is that the spectra of the *TM* samples are very similar to those of the *KN* samples. It should be remembered that discussing the X-ray diffraction measurements, which also presented some similarities between the spectra of the *TM* and *KN* samples, it was concluded that interaction between the components occurs even by simple mixing their powders in Turbula at room temperature. In that case, alongside the similarities, appreciable differences remained between the diffraction spectra of *TM* and *KN* samples of identical composition because the X-rays "see" a sample thickness greater than that which the FT-IR technique used "sees" and provide information on the bulk phases as well as on the surface phases of the samples. If the interaction between the components occurs as a result of simple mixing of the same, the *TM* and *KN* samples of identical composition differ from each other for the structure of the "bulk", not for that of the surface and the FT-IR technique used here "sees" them substantially identical. A further feature of all the compositions is the substantial disappearance of the C-H stretching vibration attributable to pure *B* (3024 cm^{-1}), which demonstrates how *B* was subject to interaction in all the samples.

The main differences between the absorption spectra of the *TM*/*KN* samples with composition $x_Z = 0.25$ and those of the pure components are recorded in the spectral range 3600 - 3300 cm^{-1} (Figure S2), a region in which the pure components do not absorb while the *TM*/*KN* samples show a large and consistent absorption band. This is the stretch absorption region of the O-H bond. Within the band, no specific absorption peaks are distinguished and therefore no hypotheses can be proposed

about the molecular conformations responsible for the absorption itself. However, it can be stated with reasonable certainty that the absorption is due to a widespread network of hydrogen bonds that is established between *Z* and *B*. The involvement of *Z* in the formation of a network of hydrogen bonds is confirmed by the spectral differences that are recorded in relation to the stretching vibrations of the C = O carboxylic (1699 cm^{-1}) and ketonic (1663 cm^{-1}), functional groups. In the pure component the two absorptions appear as distinct peaks (Figure S2) while in the samples *TM*/*KN* the absorption of the carboxyl group is no longer visible as a peak and appears as a shoulder to the left of the absorption of the ketone group which, in turn, is shifted towards higher wave numbers. These results confirm the conclusion already proposed on the basis of the discussion of X-ray diffraction measurements, according to which the interaction between pure components leads to the formation of a new phase, only at the surface level in the case of *TM* samples, and also at the bulk level in the case of *KN* samples. This phase corresponds to the co-crystals *CC1* predicted by our thermodynamic model.

The *TM*/*KN* samples of composition x_Z = 0.66 show stretching vibrations of the carboxylic and ketonic C = O (Figure S3) in all similarities to those discussed for the samples of composition x_Z = 0.25, showing that also in these samples the component *Z* is involved in a network of hydrogen bonds. The absorption spectra, on the other hand, are consistently different in the high energy region, in which the samples of composition x_Z = 0.66 do not show any absorption band for wave numbers higher than 3100 cm^{-1} (Figure S3). Also in this case it is not possible to hypothesize about the structure of the hydrogen bonds responsible for the spectral characteristics described. However, it can be affirmed with certainty that this structure is somewhat different from that of the samples with composition x_Z = 0.25. In this case too the conclusion that can be drawn is consistent with the one drawn from the X-ray diffraction measurements: the samples x_Z = 0.66 consist of a new crystalline phase, different from that of which the samples x_Z = 0.25 are made. This phase is formed, albeit only at the surface level, also in *TM* samples and corresponds to the *CC2* co-crystals predicted by our thermodynamic model.

In the samples *TM*/*KN* x_Z = 0.80 the absorption of the carboxylic group of *Z* is clearly visible as a peak even if its relative intensity is decreased compared to that of the ketone group (Figure S4). The shift towards high wave numbers of the absorption of the latter group is lower than that observed in the previous cases. Unlike the case of x_Z = 0.66, there is an appreciable absorption between 3300 and 3100 cm^{-1} (Figure S4), but not between 3600 and 3300 cm^{-1} as happened for the samples x_Z = 0.25. Furthermore, the absorption band between 3300 and 3100 cm^{-1}, which is the only spectral characteristic that differentiates the samples of composition x_Z = 0.80 from those of composition x_Z = 0.66, appears very similar to that of the pure *Z* component. The conclusion that can be drawn is that the samples of composition x_Z = 0.80 are constituted by *CC2* and pure *Z*, as indicated by the diffraction measurements and predicted by our thermodynamic model.

3.4. NMR MEASUREMENTS

To further support the diffraction results, NMR spectra have been acquired for selected samples. Figure S5 (see supplementary material) shows the ^{13}C solid state NMR spectra obtained for the *KN* samples x_Z = 0.25, x_Z = 0.66 and x_Z = 0.80, for the *TM* sample x_Z = 0.25 and for the two pure compounds *Z* and *B*. The spectra of *Z* and *B* present sharp resonances, confirming the crystalline nature of the two pure compounds, in good agreement with the DSC and XRPD observation. The assignments for the two compounds are reported in Figure S5 and have been based on previous literature and calculated spectra; spinning sidebands are marked with stars.[27,28]

The ^{13}C spectrum of *KN* x_Z = 0.25 shows sharp signals in the same chemical shift regions of the pure *Z* and *B* compounds but significant shifts can be observed; the experimental spectra can thus confirm the crystalline nature of the *KN* x_Z = 0.25 sample. This spectrum is not given by the simple superposition of the data obtained for the pure *Z* and *B* compounds, confirming the formation of new crystal structures without impurities. On the basis of the DSC and XRPD data, this new crystal phase can be identified as the *CC1*.

A similar spectrum has been obtained for the *KN* x_Z = 0.66 for which sharp resonances are observed, but the overall spectrum is not simply given by the deconvolution of the spectra of the two end-members. The comparison of *KN* x_Z = 0.25 and *KN* x_Z = 0.66 data reveals high similarities (as with the XRPD patterns) but also significant differences of chemical shifts. The more evident changes in the chemical shift values are observed for the C_7 and C_{16} for the *Z* compound, and C_a for the *B* component. Both these signals are shifted upfield. These are expected to be the groups involved in the strongest interaction in the pure *Z* and *B* compounds respectively, as the C=O, COOH and N can be involved in the formation of a H-bond network, as already reported for similar cases.[27,29] The observed shift at higher field in the *KN* samples x_Z = 0.25 and x_Z = 0.66 with respect to the pure *Z* compound can suggest a radical change in the H-bond network. The comparison of the two samples does not evidence strong differences in the chemical shift of the signals in the 170-200 ppm and 10-60 ppm regions, while some differences in peak resolution, position and relative intensities can be appreciated in the region of the aromatic carbons (110-160 ppm). This suggests that for both the co-crystals the newly formed interaction network is very similar respect to the pure *Z* and *B* compounds, and that the two co-crystals mainly differ in the interaction among the aromatic rings. Thus, it must be concluded that the crystal phase observed in the *KN* sample x_Z = 0.66 sample is different from both the *Z*, *B* and *CC1*, and it is compatible with the *CC2* identified by DSC and diffraction measurements. The evaluation of the conformation of the *Z* and *B* units in the co-crystals cannot be deduced from the NMR data.

Finally, in the spectra obtained for the *KN* x_Z = 0.80 sample many of the resonances are doubled; an accurate comparison with the pure *Z* and *KN* x_Z = 0.66 samples shows a clear superposition of the signals of the *KN* x_Z = 0.80 spectrum with both of these species (the pure compound and the co-crystals), further supporting the hypothesis that the *KN* x_Z = 0.80 sample consists of a eutectic composition of *CC2* and excess *Z* component.

To further confirm the formation of the cocrystals in the *KN* samples, the *TM* x_Z = 0.25 composition was analyzed, the results of which are also reported in Figure S5. We notice that the spectrum

matches the superposition of *Z* and *B* spectra, suggesting that no interaction occurred between the two components. On the one hand, this result confirms the indications obtained from X-ray diffraction and FT-IR spectroscopy measurements that the manipulation of the components using the *KN* and *TM* methodologies results in different samples. However, the result appears to be in contrast with the indications of the X-ray diffraction and FT-IR measurements which identify the presence of *CC1* in the sample *TM* x_Z = 0.25, even if only at the surface level. We believe that the contrast is only apparent because it is due to the different weight that the surface and bulk properties exert on the signals used by the different investigation techniques and therefore on the sensitivity of these to the surface properties.

3.5. SOLUBILITY AND DISSOLUTION RATE

The solubilities in deionized water and in the buffer solution at pH 4.5 of pure Z and of the *KN* samples with composition x_Z = 0.25, x_Z = 0.66, x_Z = 0.80 are reported in table I. A considerable enhancement of the solubility of the drug was obtained from the new compounds, compared to *Z*, after two hours in the two different fluids considered. Also the solubility at equilibrium is higher particularly in the pH 4.5 buffer (medium that simulates the administration with food) in which the solubility of the drug is particularly low. During the test in deionized water the pH decreases progressively from about 6.8 ± 0.1 to 4.4 ± 0.2, while it remains constant (as expected) at 4.5 ± 0.1 in the pH 4.5 buffer.

Samples	Deionised water (mg/L)		pH 4.5 buffer (mg/L)	
	2 h	equilibrium	2 h	Equilibrium
Z	6.4 ± 0.4	27.3 ± 2.8	2.4 ± 0.1	2.4 ± 0.1
KN x_Z = 0.25	23.6 ± 1.5	35.6 ± 1.0	10.8 ± 1.9	23.1 ± 0.5
KN x_Z = 0.66	18.3 ± 5.6	40.9 ± 0.5	5.7 ± 0.1	24.4 ± 1.0
KN x_Z = 0.80	19.6 ± 1.3	39.1 ± 2.6	5.0 ± 1.0	24.5 ± 0.5

Table I - Solubility of *Z* and *KN* samples with composition x_Z = 0.25, x_Z = 0.66, x_Z = 0.80 in deionized water and in the pH 4.5 buffer, measured after 2 hours and at equilibrium.

The dissolution profiles depend on the pH of the medium used, but that of pure *Z* is by far the most strongly dependent (see Figure 9). The amounts of drug dissolved at 60 min in buffer at pH 4.5 are all considerably lower than those dissolved in buffer at pH 6.8 but are 13.5 times lower for pure *Z*, almost three times lower for x_Z = 0.25 and more than 3 times lower for x_Z = 0.66. This is an expected result if we consider that: a) *Z* is chemically an acid and it is expected that – other conditions being equal – it dissolves more and faster as the pH increases; b) x_Z = 0.25 and x_Z = 0.66 are co-crystals with different content of *Z* and the supramolecular interactions *Z*/*B* responsible for the formation of the co-crystal cause the acid behavior of *Z* to change.

At first glance, it may be surprising that the dissolution rate profile of *KN* x_Z = 0.80 in buffer at pH 6.8 is appreciably faster than that of x_Z = 0.66 (see Figure 9) while in water and in buffer at pH 4.5 the order is reversed and the sample *KN* x_Z = 0.66 has a faster dissolution rate profile than *KN* x_Z = 0.80. In this regard, it should be noted that: a) the sample *KN* x_Z = 0.80 consists of a eutectic mixture containing *CC2* (61% by mass) and pure *Z* (39% by mass); b) the dissolution profile of pure *Z* is the one that is most depressed as the pH decreases; c) the dissolution of *Z* in water leads to a significant acidification of the solution. In buffer at pH 6.8 the dissolution rates of *CC2* (i.e., of *KN* x_Z = 0.66) and *Z* are identical or very similar up to over 40 min and both have an approximately linear trend: the dissolution profile of *KN* x_Z = 0.80 is – in fact – the sum of the dissolution profiles of the quantities of *CC2* and free *Z* contained in the sample, which provide comparable contributions to the overall dissolution rate. To confirm this interpretation, we observe that the dissolution profile of *KN* x_Z = 0.80 slows down when that of *CC2* still has a linear trend but slows down that of pure *Z* (Figure 9).

In water, the pH passes from the value of 6.75 that the solution containing pure *Z* assumes at time zero of the measurement, to the value of 4.4 that it assumes in correspondence with the solubility equilibrium, while obviously the pH does not change following the dissolution of *Z* in buffer at pH 4.5. In both cases, the dissolution profile of *Z* is greatly slowed down, because dissolution occurs in an increasingly acidic environment in the case of water and stably acid in the case of buffer at pH 4.5. The slowdown of the dissolution profile of *Z* undergoes is, as we have seen above, much more important than that of *CC2*, so that the contribution of the pure *Z* share to the dissolution profile of the sample x_Z = 0.80 becomes very modest and the dissolution profile of the sample is substantially determined by the share of *CC2* contained in it. Since this is lower than that of the sample x_Z = 0.66 (i.e. pure *CC2*) the dissolution profiles of the sample x_Z = 0.80 are below those of the sample x_Z = 0.66 both in water and in buffer at pH 4.5.

The enhancement of the dissolution rate of the new samples can be explained also in terms of wettability and this could be ascribed to a fine molecular dispersion of the more lipophilic component *Z*, in the hydrophilic component *B*. In fact, the more soluble molecules of *B* can attract water more efficiently, thus improving the wettability of *Z* at the same time.

4. CONCLUSIONS

As for many pharmaceutical solid systems, the thermal behavior of the binary mixtures zaltoprofen/4,4' bipyridine is without any doubt very complex because of the appearance of several exothermic and endothermic peaks, different from those of the pure components, whose presence, onset temperature, intensity and area strongly depend on the system composition. Here we proved that by a proper experimental design combined with a thorough quantitative analysis of the data it is possible to reach an exhaustive comprehension of the solid phases formed and of the physico-chemical phenomena occurring in the system. According to our thermodynamic model, based on a careful qualitative analysis of the DSC traces and on an in-depth quantitative analysis of the melting enthalpies of two eutectic mixtures, *Z* and *B* can form two different co-crystals, *CC1* with

molar composition *Z*:*B* = 1:3, and *CC2* with composition *Z*:*B* = 2:1. Only *CC1* is formed for compositions with a *Z* content less than or equal to that characteristic of *CC1*, while only *CC2* is formed for compositions with a *Z* content greater than or equal to that characteristic of *CC2*. For compositions with an intermediate *Z* content between those of *CC1* and *CC2* there is a concomitant formation of both the co-crystals *CC1* and *CC2*. The goodness of our model is proved by an excellent agreement between experimental and expected melting enthalpies and is confirmed by the XRPD, FT-IR and NMR measurements which, in addition, put into evidence that the interaction between the components takes place partially already at room temperature as a consequence of their simple mixing.

References

1) Hirate K, Uchida A, Ogawa Y, Arai T, Yoda K. Non-Steroidal Anti-Inflammatory Drug, Inhibits Bradykinin- Induced Pain Responses Without Blocking Bradykinin Receptors. Neurosci Res 2006;54:288-294.

2) Santenna C, Kumar S, Balakrishnan S, Jhaj R, Ahmed SN. A comparative experimental study of analgesic activity of a novel non-steroidal anti-inflammatory molecule – zaltoprofen, and a standard drug – piroxicam, using murine models. J Exp Pharmacol 2019;11: 85-91.

3) Karagianni A, Malamatari M, Kachrimanis K. Pharmaceutical cocrystals: new solid phase modification approaches for the formulation of APIs. Pharmaceutics 2017;10:1-30.

4) Sathisaran I, Dalvi SV. Engineering Cocrystals of Poorly Water-Soluble Drugs to Enhance Dissolution in Aqueous Medium. Pharmaceutics 2018;10:1-74.

5) Bolla G, Nangia A. Pharmaceutical cocrystals: walking the talk. ChemComm 2016;52:8323-8480.

6) Berry DJ, Steed WJ. Pharmaceutical cocrystals, salts and multicomponent systems; intermolecular interactions and property based design. Adv Drug Deliv Rev 2017;117:3-24.

7) Zhang C, Xiong Y, Jiao F, Wang M, Li H. Redefining the term of “Cocrystal” and broadening its intention. Cryst Growth Des 2019;19:1471-1478.

8) Duggirala NK, Perry ML, Almarsson O, Zaworotko MJ. Pharmaceutical cocrystals: along the path to improved medicines. ChemComm 2016;52:640-655.

9) Devogelaer JJ, Meekes H, Vlieg E, De Gelder H. Cocrystals in the Cambridge Structural Database: a network approach. Acta Crystallogr Section B, Structural Science, Crystal Engineering and Materials 2019;75:371-383.

10) Walsh RDB, Bradner MW, Fleischman S, Morales LA, Moulton B, Rodriguez-Hornedo N, Zaworotko MJ. Crystal engineering of the composition of pharmaceutical phases. ChemComm 2003;2:186−187.

11) Surov AO, Solanko KA, Bond AD, Bauer-Brandl A, Perlovich GL. Polymorphism of felodipine co-crystals with 4,4'-bipyridine. CrystEngComm 2014;16:6603−6611.

12) Oswald IDH, Allan DR, McGregor PA, Motherwell WDS, Parsons S, Pulham CR. The formation of paracetamol (acetaminophen) adducts with hydrogen-bond acceptors. Acta Crystallogr Sect. B 2002;58:1057−1066.
13) Surov AO, Simagina AA, Manin NG, Kuzmina LG, Churakov AV, Perlovich GL. Fenamate Cocrystals with 4,4'-Bipyridine: Structural and Thermodynamic Aspects. Cryst Growth Des 2015;15:228-238.
14) Karimi-Jafari M, Padrela L, Walker GM, Croker DM, Creating Cocrystals: A Review of Pharmaceutical Cocrystal Preparation Routes and Applications. Cryst Growth Des 2018;18:6370−6387.
15) Malamartari M., Ross S.A., Douroumis D., Velaga S.P. Experimental cocrystal screening and solution based scale-up cocrystallization methods. Adv Drug Deliv Rev 2017;117: 162-177.
16) Steed JW, The role of co-crystals in pharmaceutical design, Trends in Pharmacol Sci 2013;34:185-193.
17) Yamashita H, Hirakura Y, Yuda M, Teramura T, Terada T. Detection of cocrystal formation based on binary phase diagrams using thermal analysis. Pharm Res 2013;30:70-80.
18) Yamashita H, Hirakura Y, Yuda M, Terada K. Coformer screening using thermal analysis based on binary phase diagrams. Pharm Res 2014;31:1946–57.
19) Manin AN, Voronin AP, Drodz KV, Manin NG, Bauer-Brandim A, Perlovich L. Cocrystal screening of hydroxyenzamides with benzoic acid derivatives: a comparative study of thermal and solution-based methods. Eur J Pharm Sci 2014;65:56-64.
20) Zhou Z, Chan HM, Sung HHY, Tong HHY, Zheng Y. Identification of new cocrystal systems with stoichiometric diversity of salicylic acid using thermal methods. Pharm Res 2016;33:1030-9.
21) Saganowska P, Wesolowski M. DSC as a screening tool for rapid co-crystal detection in binary mixtures of benzodiazepines with co-formers. J Therm Anal Cal. 2018;133:785-795.
22) Park B, Yoon W, Yun J, Ban E, Yun H, Kim A. Emodin-nicotinamide (1:2) cocrystal identified by thermal screening to improve emodin solubility. Int J Pharm. 2019;557:26-35.
23) Zaltoprofen/Official Monographs, The Japanese Pharmacopoeia, JP 17th ed., Shibuya-ku, Tokyo, Japan, 2016, pp. 1780-81.
24) Bruni G, Maggi L, Mustarelli P, Sakaj M, Friuli V, Ferrara C, Berbenni V, Girella A, Milanese C, Marini A, Enhancing the pharmaceutical behavior of nateglinide by cocrystallization: physicochemical assessment of cocrystal formation and informed use of differential scanning calorimetry for its quantitative characterization. J Pharm Sci 2019;108:1529-1539.
25) Bruni G, Monteforte F, Maggi L, Girella A, Berbenni V, Milanese C, Marini A. Probenecid and benzamide: DSC applied to the study of an impossible system. J Therm Anal Cal. 2020 doi.org/10.1007/s10973-020-09749-x.
26) Dash SG, Thakur TS. Computational screening of multicomponent solid forms of 2-aryl-propionate class of NSAID, zaltoprofen, and their experimental validation. Cryst Growth Des. 2021;21:449-461.

27) Li S, Lin X, Xu K, He J, Yang H, Li H. Co-grinding Effect on Crystalline Zaltoprofen with β-cyclodextrin/Cucurbit[7]uril in Tablet Formulation**.** Sci Rep. 2017;7:45984.
28) http://www.molbase.com/en/hnmr_553-26-4-moldata-15461.html
29) Sherje AP, Patel F, Murahari M, Suvarna V, Patel K. Study on effect of L-arginine on solubility and dissolution of Zaltoprofen: Preparation and characterization of binary and ternary cyclodextrin inclusion complexes. Chem Phys Lett. 201 8;694:120-128.

Legends

Figure 1. DSC traces of *TM* (a, b) and *KN* (a*, b*) samples of different composition. a), a*): x_Z = 0,10; b), b*): x_Z = 0,40. x_Z is the molar fraction of component Z.

Figure 2. DSC traces of *TM* (a – d) and *KN* (a* - d*) samples of different composition. a), a*): x_Z = 0,50; b), b*): x_Z = 0,60; c), c*): x_Z = 0,80; d), d*): x_Z = 0,90. x_Z is the molar fraction of component *Z*.

Figure 3. Tammann's plot for the *EU2* melting peak. Experimental values obtained for *TM* samples and their linear interpolation (red); values expected under the assumption that *Z* and *B* form a simple eutectic phase diagram and their linear interpolation (black). The expected values were calculated using equations 1 and 2 (see text)**.**

Figure 4. Tammann's plot for the *EU2* melting peak. Experimental values obtained for *TM* samples and their linear interpolation (red); expected values and their linear interpolation for mixtures not affected by the thermodynamic constraint (black); expected values for mixtures affected by the thermodynamic constraint and their linear interpolation (green).

Figure 5. Tammann's plot for *EU4* melting peak. Red circles and red lines: experimental values ($\Delta \boldsymbol{H}_{\boldsymbol{EU4}}^{\boldsymbol{meas}}$) and their linear interpolation; black circles and black lines: expected values ($\Delta \boldsymbol{H}_{\boldsymbol{EU4}}^{\boldsymbol{exp}}$) and their linear interpolation.

Figure 6. XRPD patterns of *Z* (a); *TM* x_Z = 0.25 (b); *KN* x_Z = 0.25 (c) and *B* (d).

Figure 7. XRPD patterns of *Z* (a); *TM* x_Z = 0.66 (b); *KN* x_Z = 0.66 (c); *B* (d) and the simulated XRPD pattern of *CC2* (e).

Figure 8. XRPD patterns of *Z* (a); *TM* x_Z = 0.80 (b); *KN* x_Z = 0.80 (c) and *B* (d).

Figure 9. Dissolution profiles of pure *Z*, *KN* x_Z = 0.25*, KN* x_Z = 0.66 *and KN* x_Z = 0.80 samples in the three different media considered: buffer at pH = 6.8, deionized water and buffer at pH = 4.5.